Spectral roughness of glaciated bedrock geomorphic surfaces: Implications for glacier sliding

JOURNAL OF GEOPHYSICAL RESEARCH, VOL. 105, NO. B9, PAGES 21,295–21,303, SEPTEMBER 10, 2000

Spectral roughness of glaciated bedrock geomorphic surfaces: Implications for glacier sliding

Bryn Hubbard

Centre for Glaciology, Institute of Geography and Earth Sciences, University of Wales, Aberystwyth United Kingdom

Martin J. Siegert

Bristol Glaciology Centre, School of Geographical Sciences, University of Bristol, Bristol England, United Kingdom

Danny McCarroll

Department of Geography, University of Wales, Swansea, Swansea, United Kingdom

Abstract. A microroughness meter (MRM) was used to measure the high-frequency roughness of a number of geomorphic surfaces in the forefield of Glacier de Tsanfleuron, Switzerland. Resulting spectral power densities are added to low-frequency spectra, measured by electro-optical distance meter (EDM), to generate composite roughness spectra that include almost 5 orders of magnitude of roughness in the frequency domain. These are used to define two roughness indices: a general index of bed roughness is defined as the integral of the raw, spectral power densities, and a sliding-related index of bed roughness is defined as the integral of the spectral power densities weighted to account for the optimum dependence of glacier sliding speed on hummock wavelength. Results indicate that MRM-measured geomorphic components vary in roughness by 3 orders of magnitude, principally depending on the surface microenvironment measured and profile orientation relative to the direction of former ice flow. Both MRM- and EDM-measured roughnesses are lower parallel to the direction of former ice flow than perpendicular to it. Composite roughness spectra consequently indicate that the glacier bed is smoothed in the direction of former ice flow at all horizontal scales from 1 mm to 40 m, typically resulting in an order of magnitude decrease in sliding-related roughness relative to that measured perpendicular to ice flow. Comparison of data from two survey sites located adjacent to, and ~1.2 km from, the current glacier margin indicates that postglacial subaerial weathering homogenizes bedrock roughness, in particular reducing high-frequency, flow-orthogonal roughness. Accounting for the effect of 28% ice-bedrock separation over one of the profiles reduces net, sliding-dependent roughness by between 27% and 43%, depending on the transition wave number used.

1. Introduction

Subglacial abrasion is generally believed to reduce bedrock roughness parallel to the direction of ice flow [e.g., *Boulton,* 1979]. This assertion, however, is largely based on qualitative observations, or on field measurements at a horizontal resolution of at least some centimeters and a vertical resolution of at least some millimeters [e.g., *Benoist,* 1979; *Sharp et al.,* 1989]. With the notable exception of a small number of studies based on single profiles [e.g., *Echelmeyer and Zhongxiang,* 1987; *Cuffey et al.,* 1999], the small-scale roughness of glacier beds remains quantitatively unconstrained at the subcentimeter scale, despite the potential for roughness at this scale to exert strong control over glacier sliding speed [e.g., *Nye,* 1970; *Kamb,* 1970] and erosion [e.g., *Hallet,* 1979a]. Beneath temperate glaciers this basal motion is accomplished by pressure-induced melting and refreezing (regelation) cycles, which operate most effectively around small-scale bedrock bumps, and enhanced ice deformation, which operates most effectively around larger bedrock irregularities [*Weertman,* 1957, 1964]. The two processes combine to define a bedrock hummock transition wavelength that exerts the greatest resistance to basal sliding. Theoretical considerations indicate that this transition wavelength is of the order of 0.1 to 1 m [e.g., *Kamb,* 1970], with ice moving more easily around shorter roughness elements by regelation and around longer roughness elements by enhanced deformation. It is therefore important for the empirical evaluation of sliding theory that bedrock roughness be measured in the field at scales that fully bracket this transition wavelength and over the full range of bed surfaces present. This requirement, however, introduces the problem of measuring millimeter- or submillimeter-scale, high-frequency roughness over profiles that include low-frequency elements that are some meters to tens of meters long.

One solution to this problem lies in the recognition that glacier beds may be described in terms of a number of

Paper number 2000JB900162.
0148-0227/00/2000JB900162$09.00

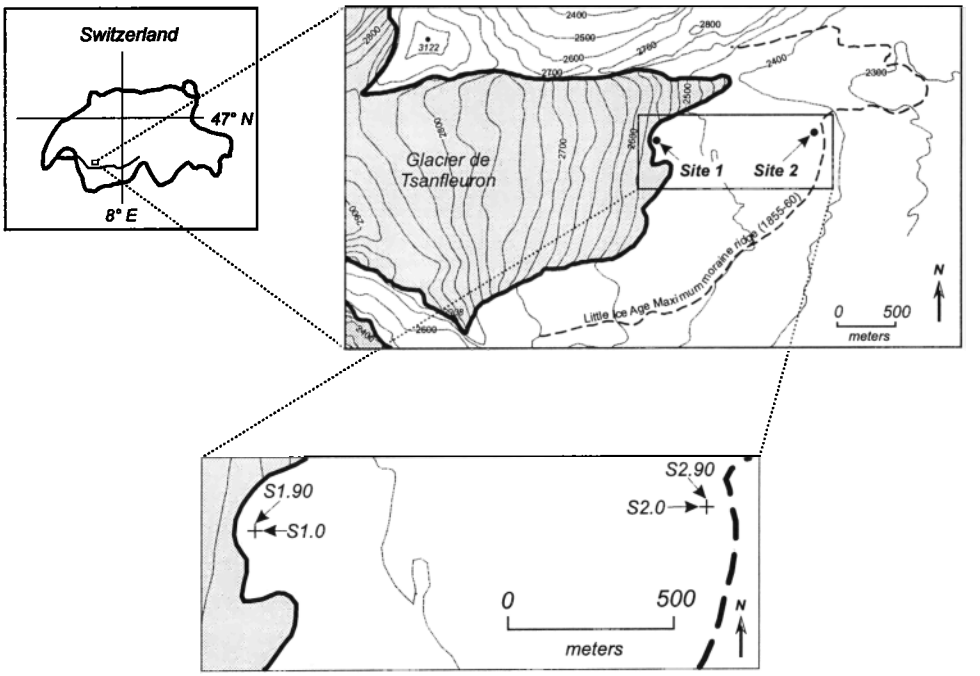

Figure 1. Location of Glacier de Tsanfleuron, Switzerland, and of bedrock roughness profiles referred to in the text.

distinctive, geomorphic components, each defined on the basis of a common mode of formation, whether erosional or depositional. Such components could be defined on the basis of the nature of the surface concerned, including, for example, incised channels [e.g., *Nye*, 1973], cavities, abraded bedrock surfaces, precipitate-covered bedrock surfaces [e.g., *Hallet*, 1976], and unconsolidated sedimentary surfaces. Given a distinctive origin for each such component, it is highly likely that each will also be characterized by a correspondingly distinctive roughness signature, particularly at high frequency. It may therefore be possible to characterize the net roughness of any glacier bed in terms of the roughness of its constituent geomorphic components. The adoption of such an approach is significant, since it allows a small number of high-resolution roughness measurements to be generalized up to larger spatial scales (or even to other field sites) without having to repeat the small-scale roughness measurements over the entire length of the profiles considered. In the present study we attempt such an approach based on field measurements on massive limestone bedrock exposed by the post-Little Ice Age (LIA) retreat of Glacier de Tsanfleuron, Switzerland (Figure 1).

2. Field Site and Methods

Glacier de Tsanfleuron has a surface area of ~4 km^2 and extends from ~2420 to ~2850 m above sea level northwest of Sion, Switzerland (Figure 1). The glacier has been widely studied, mainly in terms of the relationship between its basal ice layers [*Hallet et al.*, 1978; *Lemmens et al.*, 1982; *Souchez and Lemmens*, 1985; *Tison and Lorrain*, 1987; *Hubbard and Sharp*, 1995] and the carbonate crusts [e.g., *Hallet*, 1976, 1979b] deposited on the Urgonian (Cretaceous) limestone bedrock exposed by its post-Little Ice Age retreat [e.g., *Sharp et al.*, 1990; *Fairchild et al.*, 1993; *Hubbard and Hubbard*, 1998].

The present study site is located on this limestone plateau (Figure 1). Bedrock roughness profiles were measured at different scales by electro-optical distance meter (EDM) and by microroughness meter (MRM) [*McCarroll*, 1992]. Measurement and processing procedures were as follows:

1. Four profiles, each 40 m long, were measured by EDM at a horizontal point spacing of 0.1 m along each profile. Profiles were measured parallel and perpendicular to the former ice flow direction at two sites: Site 1 is located within 100 m of the current ice margin, and Site 2 is located just within the LIA moraine ~1.2 km downflow (Figure 1). Four, 400-point, EDM profiles were thereby recorded: site 1 flow-parallel (labeled S1.0), site 1 flow-orthogonal (S1.90), site 2 flow-parallel (S2.0), and site 2 flow-orthogonal (S2.90) (Figure 2). The vertical and horizontal resolution of these measurements is ~1 mm [*Geotronics Limited*, 1995].

2. Each EDM-measured bedrock profile was logged in terms of a fourfold classification of the principal surface geomorphic components identified in the proglacial area. These were striated bedrock (labeled Sb), striated bedrock with surface sparite carbonate deposit (SbS), former basal cavity with no surface deposit (Ca), and former basal cavity with surface micrite carbonate deposit (CaM) (Figure 3 and Table 1). Basal cavities were defined as all areas of the glacier that were inferred (from bedrock color, an absence of striations and geometrical considerations) to have been separated from base of the overlying glacier (e.g., Figure 3a). This category therefore includes the linked cavity system present beneath the glacier [*Sharp et al.*, 1989], including former Nye channels, as well as relatively isolated water-filled cavities. Bedforms such as chattermarks were rarely observed and, where encountered, the local roughness of chipped and pitted bedrock was included within the existing classification depending on location (Sb or Ca) and surface character (no coating, S or M). Sparite is generally composed of relatively

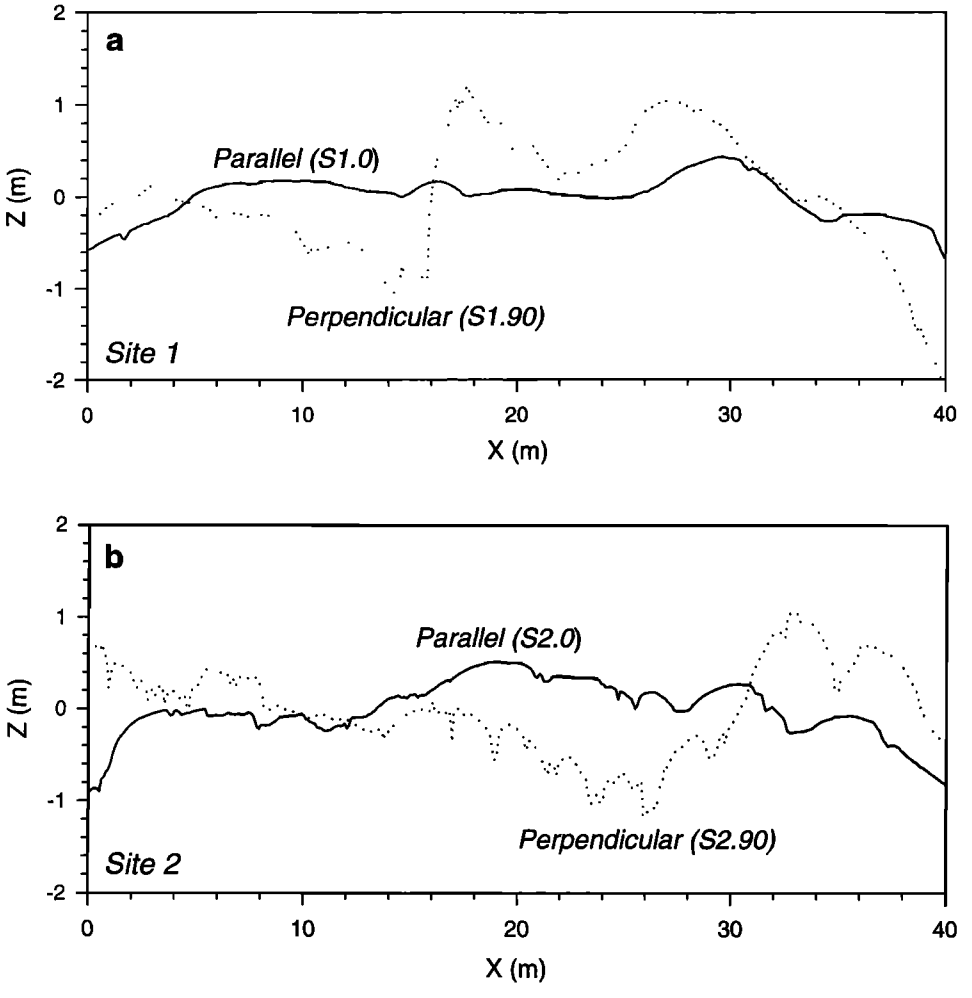

Figure 2. Raw EDM-measured bedrock roughness profiles measured over 40-m lengths at a horizontal spacing of 0.1 m at (a) site 1 and (b) site 2.

large, elongate calcite crystals that are aligned parallel to the former iceflow direction, and micrite is finer-grained, forming surfaces that are smooth or gently undulating [*Sharp et al.*, 1990; *Hubbard and Hubbard*, 1998]. All four components were observed at site 1, but only three were observed at site 2, from where CaM was absent.

3. Four profiles, each 0.1 m long, were measured at a horizontal spacing of 1 mm by MRM over each of the surface geomorphic components identified. Such profile sets were measured both parallel and perpendicular to the former ice flow direction at both sites 1 and 2 (Figure 4). Fifty-six, 100-point MRM profiles were therefore measured, 32 (4 samples x 4 components x 2 orientations) at site 1, and 24 (4 samples x 3 components x 2 orientations) at site 2 (Table 1). The resolution of these MRM measurements is ~0.01 mm [*McCarroll*, 1992].

4. All EDM- and MRM-measured roughness profiles were detrended by least squares linear regression and transformed into the frequency domain by calculating the discrete Fourier transform of their autocorrelation function [*Cooley and Tukey*, 1965]. The four MRM-measured profiles in each microenvironment were averaged in the frequency domain for each location. The resulting data are presented as bivariate plots of spectral power density, $S(k)$ (m^3), against wave number (m^{-1}), given as (2π/[wavelength in m]). Following *Nye* [1970], the normalized spectral power density $S(k)$ is defined as

$$S(k) = \lim_{l \to \infty} \frac{1}{l} \left| \overline{z_0}(k) \right|^2, \quad (1)$$

where l is the profile length and $\left| \overline{z_0}(k) \right|^2$ is the raw Fourier series transform.

5. Mean MRM-measured spectral power densities for each microenvironment were weighted by their coverage as indicated by the 40-m-long profile logs. These were then added to the EDM-measured power spectra to create composite power spectra covering the full range of scales recorded for each of the four 40-m-long profiles (Figures 5a and 5b).

6. The relative resistance presented by individual roughness profiles to basal sliding was evaluated following *Nye's* [1970] sliding theory, where basal sliding velocity (V) is given as

$$V = \frac{\tau}{\left[\left(2\eta k_*^2 / \pi \right) \int_0^\infty dk \; S(k) W(k) \right]}, \quad (2)$$

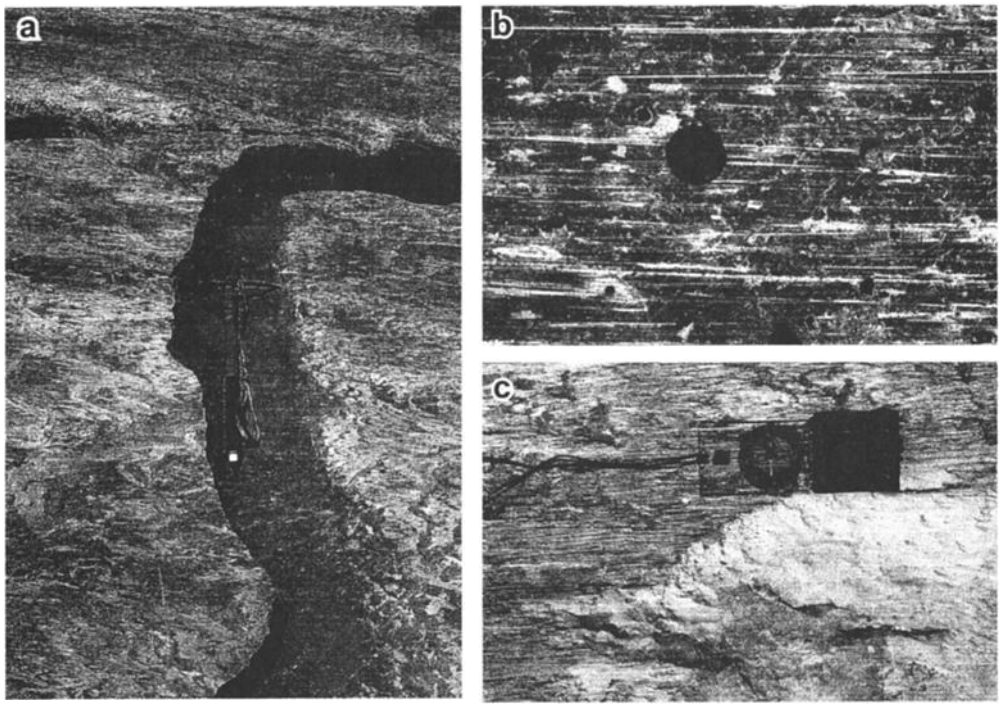

Figure 3. Examples of geomorphic surface components defined in the study. (a) Striated bedrock intermittently coated with sparite deposit (lighter) spanning an uncoated former basal cavity (center of plate, containing ice axe for scale). (b) Uncoated striated bedrock located near the current glacier margin. (c) Bedrock with a thick sparite coating (left of plate) contrasts with smoother, micrite-coated former cavity (right of plate). The former ice flow direction was left to right in each case.

where τ is the basal driving stress, η is the effective viscosity of the ice, k is the wave number, $S(k)$ is the normalized spectral power density, and $W(k)$ is a weighting function, given by $k^3(k_*^2 + k^2)^{-1}$, where the constant k_* is the transition wave number (the wave number equivalent of the transition wavelength). While sliding velocity can potentially be calculated from equation (2), this is not done in the present study because *Nye's* [1970] assumption of universal ice-bedrock contact (no ice-bed separation) is clearly violated: Between 28 and 60% of the individual profiles are characterised by ice-bedrock separation (Table 1). Indeed, no currently formulated basal sliding theory accounts explicitly for the influence of both ice-bed separation and bed roughness. While equation (1) cannot, therefore, be used to predict V, two measures of the bedrock roughness can be defined based on the integral in the denominator. First, we define a total bedrock roughness index (ξ) as the integral of the normalized spectral power density:

$$\xi = \left(\int_0^\infty dk\ S(k) \right); \tag{3}$$

ξ thereby provides a summary measure of the full range of roughness elements present in our spectral power density plots (Fig. 5a and 5b). Second, we define a sliding-related bedrock roughness index (ζ) as the integral of the weighted normalised spectral power density (Fig. 5c and 5d):

$$\zeta = \left(\int_0^\infty dk\ S(k)W(k) \right); \tag{4}$$

ζ thereby provides a summary measure of the full range of roughness elements present in our weighted spectral power density plots (Figures 5c and 5d), approximating the drag exerted by the glacier bed on the overlying ice. The values of ξ (Figure 6) and ζ are calculated for a variety of roughness profiles for $k_* = 6.3\ m^{-1}$ (equating to a transition wavelength of 1.0 m). Results are summarized in Table 2.

Roughness indices calculated by equations (3) and (4) increase with the spatial scale of the profiles measured. Calculated values of ξ and ζ are therefore only universally comparable if roughness is measured over profiles composed of the same range of wavelengths. Roughnesses in the present study are therefore comparable within each profile group

Table 1. EDM Profile Logs as Percentage Cover of Geomorphic Components Measured at Sites 1 and 2, Parallel (0) and Perpendicular (90) to Former Ice Flow Direction

Surface Environment*	Site 1 (0), %	Site 1 (90), %	Site 2 (0), %	Site 2 (90), %
Sb	43.2	37.5	40.0	41.0
SbS	28.8	34.1	0.0	0.0
Ca	20.5	25.8	60.0	59.0
CaM	7.5	2.6	0.0	0.0

* Striated bedrock (Sb), striated bedrock with surface sparite deposit (SbS), former basal cavity (Ca), and former basal cavity with surface micrite deposit (CaM).

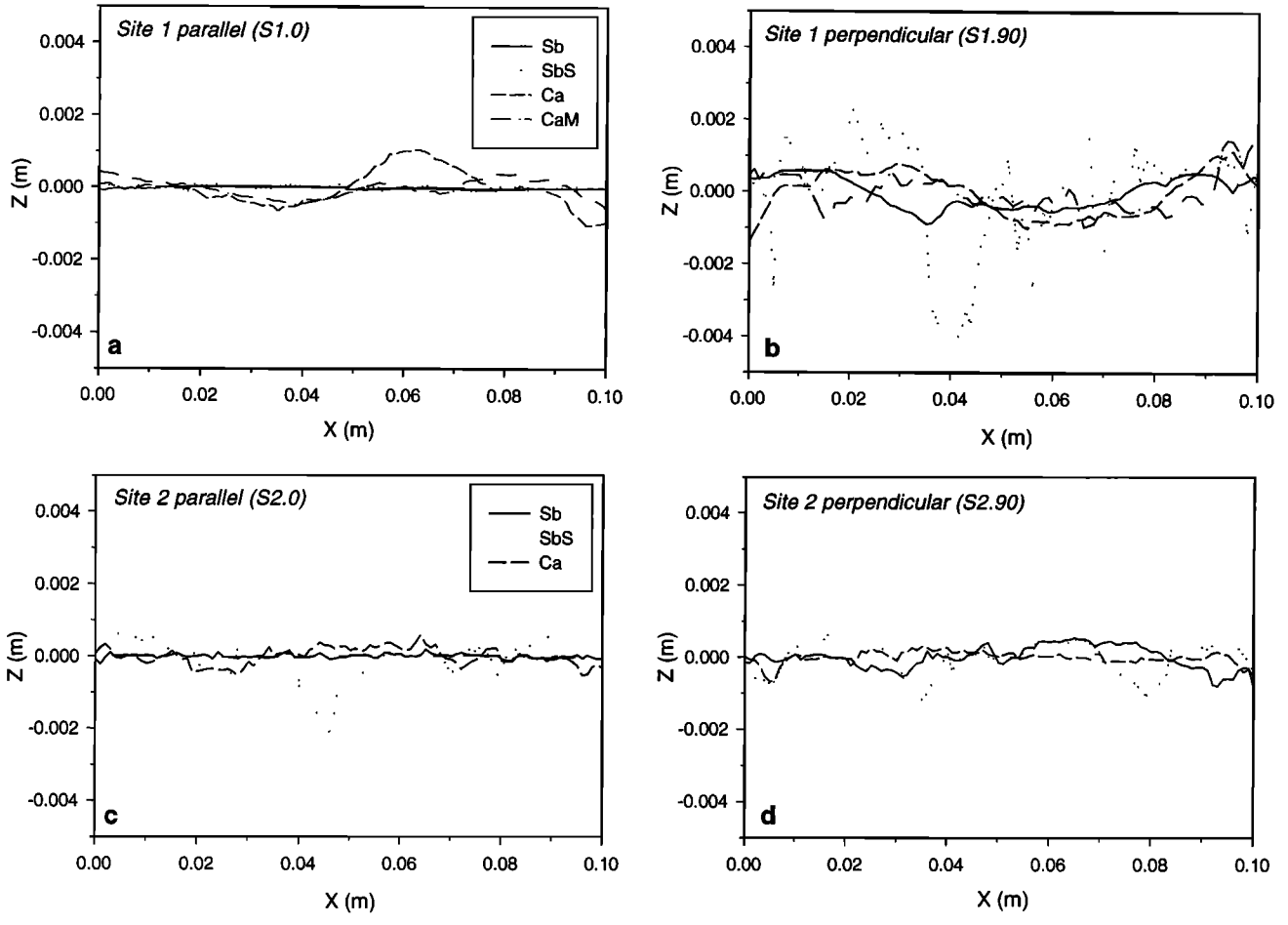

Figure 4. Representative raw surface profiles measured by microroughness meter at sites 1 (S1) and 2 (S2) recorded parallel (0) and perpendicular (90) to the former ice flow direction. Labels for surface geomorphic components are striated bedrock (Sb), striated bedrock with sparite precipitate coating (SbS), former cavity with no surface deposit (Ca), and former cavity with micrite precipitate coating (CaM). Four examples of each such profile were measured in the field.

(EDM-only, MRM-only, and composite spectra), but not between groups.

7. The effects of ice-bed separation were evaluated for the composite profile aligned parallel to the former ice flow direction at site 1 (S1.0) by replacing bedrock hollows logged as former cavities with straight lines joining the upflow and downflow points of ice-bedrock separation. All roughness contained within these sections was thereby removed from the analysis. Results are illustrated in Figure 7 and summarized in Table 2.

8. The effects of the transition wave number (k_*) adopted in the analysis are evaluated for all composite profiles. Weighted spectral power density is calculated assuming a relatively high value of k_* (63 m^{-1}, equivalent to a transition wavelength of 0.1 m) and compared with that generated for the standard runs (k_* = 6.3 m^{-1}). Results are illustrated in Figure 8 and summarized in Table 2.

3. Results and Interpretation

3.1. EDM-Measured Roughness

Raw EDM-measured roughness profiles (Figure 2) indicate that surfaces are smoother parallel to the former ice flow direction than perpendicular to it, even at this relatively coarse scale. While this holds for both sampling sites, the difference appears to be more pronounced close to the glacier margin (S1) than just within the Little Ice Age (LIA) moraine (S2). Calculated values of ξ (Table 2) support this pattern, increasing from 1.01 for the flow-parallel profile at site 1 (S1.0), to 1.91 for the flow-parallel profile at site 2 (S2.0), to 7.78 for the flow-orthogonal profile at site 2 (S2.90), to its maximum value of 12.73 for the flow-orthogonal profile at site 1 (S1.90).

3.2. MRM-Measured Roughness

MRM-measured profiles at site 1 include all four geomorphic components: striated bedrock (Sb); striated bedrock with sparite coating (SbS); former cavity (Ca), and former cavity with micrite coating (CaM). The resulting profiles are particularly smooth measured parallel to the direction of former ice flow, registering a maximum vertical deviation of <1 mm over the 0.1-m-long profiles (Figures 4a and 4b). In contrast, flow-orthogonal MRM-measured profiles are markedly rougher than the flow-parallel profiles, particularly at site 1. The raw, flow-orthogonal profile over striated bedrock with sparite coating at site 1 (S1.90SbS) is

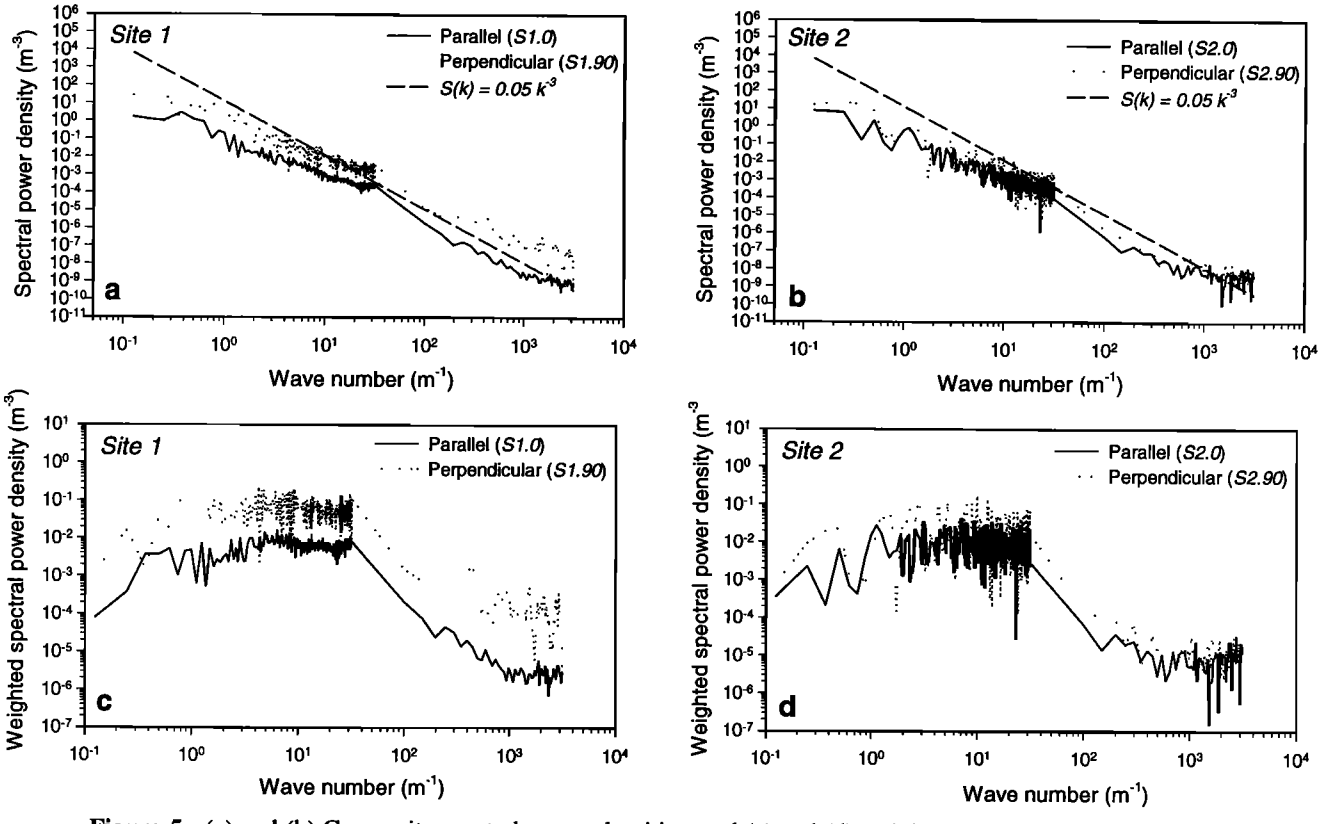

Figure 5. (a) and (b) Composite spectral power densities, and (c) and (d) weighted spectral power densities of profiles measured at sites 1 and 2 respectively. The relation for white roughness (n = 3 in equation (5)) is presented for comparison in Figures 5a and 5b. Best fit regression values of A and n (equation (5)) for the data presented in Figures 5a and 5b are given in Table 3.

markedly rougher than any other profile measured, being characterized by a maximum vertical deviation of >4 mm (Figure 4b). This extreme small-scale roughness reflects the elongate and furrowed nature of the surface sparite deposits (Figure 3c). Values of the net roughness index (ξ) calculated for four examples of each of these MRM-measured profiles (Figure 6) define characteristic roughness ranges that support this pattern. Site 1, MRM-measured profiles reveal 3 orders of magnitude variability in ξ, from 2.2 x 10^{-6} over striated bedrock measured parallel to flow (S1.0Sb), to 2.1 x 10^{-3} over striated bedrock with sparite coating measured perpendicular to flow (S1.90SbS) (Table 2). Indeed, calculated roughness at site 1 is lower parallel to the direction of former ice flow than perpendicular to it for each of the individual subglacial environments measured (Figure 6 and Table 2). Since site 1 has been exposed by glacier retreat for <15 years, these patterns are inferred to reflect accurately the immediate effects of subglacial erosion (and deposition in the case of the precipitate-covered surfaces), with only minimal alteration by postglacial subaerial weathering.

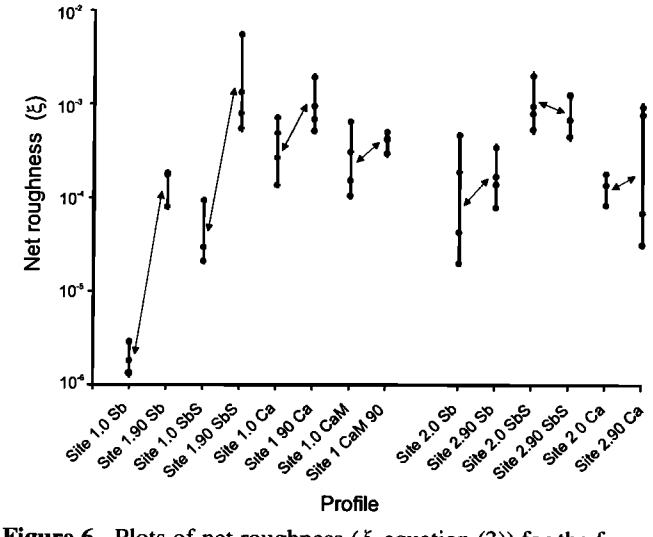

Figure 6. Plots of net roughness (ξ, equation (3)) for the four examples of each geomorphic component measured in the field. Double-ended arrows connect mean roughness data from flow-parallel and flow-orthogonal profiles over the respective geomorphic components. Notations are defined in the text.

MRM-measured profiles recorded at site 2 include only three geomorphic components (Sb, SbS, and Ca), since no micrite deposits were observed at this location. The resulting profiles are generally less varied than those measured at site 1, irrespective of orientation (Figures 4c, 4d, 6 and Table 2). Site 2 MRM profiles are generally rougher than their equivalent geomorphic components recorded parallel to former ice flow direction at site 1 and smoother than their equivalent geomorphic components recorded perpendicular to former ice flow direction at site 1. Thus site 2 MRM-only ξ values range from 1.9 x 10^{-4} for S2.0Sb, to 9.4 x 10^{-4} for S2.0Sbs. In the case of the latter value, it is notable that the roughest MRM-measured profiles at site 2 are over striated bedrock with sparite coating irrespective of orientation. These patterns are consistent with the relatively nonorientation-specific nature of

Table 2. Summary Bedrock Roughness Data

Orientation	Surface Environment	ξ		ζ			
				$k_s = 6.3\ m^{-1}$		$k_s = 63\ m^{-1}$	
		Site 1 (S1)	Site 2 (S2)	Site 1 (S1)	Site 2 (S2)	Site 1 (S1)	Site 2 (S2)
		EDM Only					
Parallel (0)	full profile	1.01	1.91				
Perpendicular (90)	full profile	12.73	7.78				
		*MRM Only**					
Parallel (0)	striated bedrock (Sb)	0.22 (0.077)	18 (21)				
Parallel (0)	striated bedrock with sparite coating (SbS)	4.8 (4.0)	110 (67)				
Parallel (0)	former cavity (Ca)	41 (25)	14 (5.0)				
Parallel (0)	former cavity with micrite coating (CaM)	31 (25)	/				
Perpendicular (90)	striated bedrock (Sb)	16 (4.9)	19 (12)				
Perpendicular (90)	striated bedrock with sparite coating (SbS)	210 (230)	94 (42)				
Perpendicular (90)	former cavity (Ca)	100 (64)	47 (48)				
Perpendicular (90)	former cavity with micrite coating (CaM)	42 (8.6)	/				
		Composite (MRM and EDM)					
Parallel (0)	full profile	1.02	1.92	0.510	0.468	0.102	0.080
Parallel (0)	full profile#	1.02	/	0.374	/	0.058	/
Perpendicular (90)	full profile	12.86	7.81	6.700	1.440	1.796	0.239

Profile codes are in parentheses, as defined in the text.
* Mean values (x 10^{-5}) of four examples are presented with standard deviations (x 10^{-5}) in parentheses.
# Includes the effects of ice-bed separation; see text for explanation.

the subaerial weathering that site 2 has experienced since the glacier retreated from the site ~130 years ago. In this case, geomorphic components that were glacially smoothed at site 1 (e.g., S1.0Sb and S1.0SbS) were observed at site 2 to have become denuded and pitted by subaerial weathering. Smooth micrite deposits have been eroded from site 2 altogether (Table 1). This erosion has had the effect of increasing the flow-parallel, small-scale roughness and decreasing the flow-orthogonal, small-scale roughness at site 2 relative to the recently deglaciated bedrock at site 1 (Fig. 4).

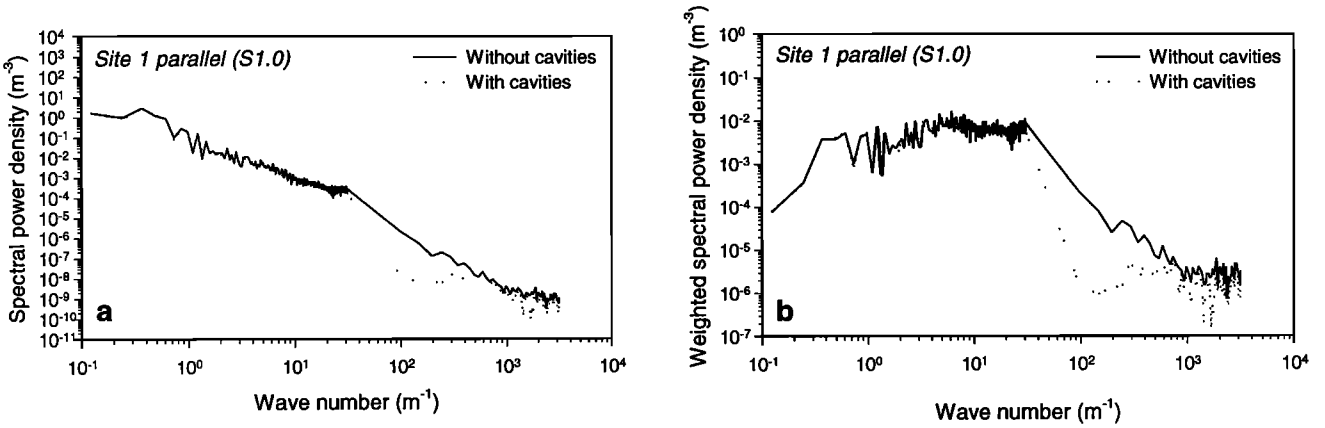

Figure 7. (a) Composite spectral power density and (b) weighted composite spectral power density of S1.0 in the presence and absence of basal cavities formed by ice-bed separation. See text for explanation.

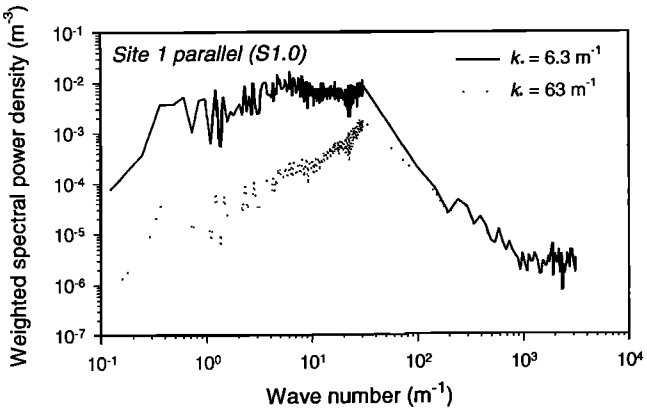

Figure 8. Weighted composite spectral power density of S1.0 with transition wave numbers (k_*) of 6.3 m^{-1} and 63 m^{-1}. See text for explanation.

3.3. Composite Roughness Spectra

Composite roughness spectra (Figure 5) represent a combination of the coarse- and fine-scale roughness measured by EDM and MRM, respectively. These plots indicate that the relationship between spectral power density ($S(k)$) and wave number (k) may be approximated by a power function of the form

$$S(k) = A\,k^{-n} \tag{5}$$

(as suggested by *Nye* [1969]), where A and n are constants. White roughness, at which roughness elements are similarly shaped at all scales, is characterized by $n = 3$. In spectra characterized by $n < 3$, roughness is greater at high frequency relative to the white roughness spectrum, and conversely. Fitting curves of this form (equation (5)) to our composite roughness spectra (Figures 5a and 5b) indicates that for the forefield of Glacier de Tsanfleuron, n lies between 2.27 (S2.0) and 2.48 (S1.0) (Table 3). This range of values encompasses that recorded by *Benoist* [1979] in the proglacial area of Glacier de Saint-Sorlin, France, where four profiles yielded a mean value of $n = 2.36 \pm 0.1$. These values contrast with that determined on the basis of small-scale bedrock roughness measured beneath Meserve Glacier, Antarctica, where *Cuffey et al.* [1999] obtained $n = 3$. Our data therefore suggest that high-frequency roughness is slightly over-represented at the bed of Glacier de Tsanfleuron (as it is at Glacier de Saint-Sorlin) relative both to a white roughness spectrum and to that measured beneath Meserve Glacier, Antarctica. However, it is worth noting that the Meserve Glacier spectra extended to wave numbers of 10^8 m^{-1}, raising the possibility that the slope of 3 measured by *Cuffey et al.* [1999] partly reflected roughness at very high wave numbers that were not included in the present study.

Values of ξ calculated for these composite roughness spectra have values of 1.02 for S1.0, 1.92 for S2.0, 7.81 for S2.90, and 12.86 for S1.90. Relative variability is markedly less than that revealed by the MRM-measured profiles recorded at each site (Figure 6 and Table 2), reflecting the dominant influence that coarse-scale roughness has over ξ. This variability is matched in calculations of the sliding-dependent roughness index (equation (4)). Calculated values of ζ ($k_* = 6.3$ m^{-1}) similarly vary by ~1 order of magnitude between flow-parallel and flow-orthogonal orientations: from 0.468 over S2.0 and 0.510 over S1.0, to 1.440 over S2.90 and 6.700 over S1.90 (Table 2). Thus a slight alteration in the direction of ice flow over these surfaces could have the effect of increasing the resistance to basal sliding significantly.

Accounting for the influence of ice-bed separation along S1.0 decreases roughness at high wave numbers (i.e., high frequency) (Figure 7). Although the dominance of low wave number roughness in the raw power spectrum minimizes the effects of ice-bed separation on net roughness (ξ), such separation does influence sliding-related roughness (ζ), since this power spectrum is preferentially weighted around the transition wave number (6.3 m^{-1}). For S1.0, therefore, the influence of (28%) ice-bed separation is to reduce the net sliding-related roughness from 0.51 in the absence of separation to 0.37, representing a decrease of ~27% (Table 2). Since other profiles are characterised by up to 60% ice-bed separation (Table 1), this reduction in ζ is likely to be at the lower end of the range for Glacier de Tsanfleuron.

The effect of increasing the transition wave number (k_*) from 6.3 m^{-1} to 63 m^{-1} is to decrease the contribution of low wave number roughness (<63 m^{-1}) to net sliding-dependent roughness (Figure 8). For example, increasing k_* for S1.0 reduces sliding-dependent roughness (ζ) by 80%, from 0.510 (at $k_* = 6.3$ m^{-1}) to 0.102 (at $k_* = 63$ m^{-1}) (Table 2). In the case of sliding with ice-bed separation, ζ is reduced from 0.374 (at $k_* = 6.3$ m^{-1}) to 0.058 (at $k_* = 63$ m^{-1}).

4. Conclusions

Analysis of composite roughness spectra, constructed by weighting the small-scale roughness of individual geomorphic components and combining these with larger-scale profiles at Glacier de Tsanfleuron, Switzerland, allows a number of conclusions to be drawn:

1. Glacier bed roughness is smoothed at all scales (from 1 mm to 40 m) in the direction of former ice flow relative to that measured perpendicular to flow.

2. High-frequency roughness of four surface geomorphic components (striated bedrock, striated bedrock with surface sparite carbonate deposit, former basal cavity with no surface deposit, and former basal cavity with surface micrite carbonate deposit) varied by 3 orders of magnitude, depending on the geomorphological component measured and profile orientation.

3. Composite roughness spectra indicate that spectral power density may be adequately described as a power

Table 3. Best Fit Parameters for Composite Profile Plots of Spectral Power Density $S(k)$ Against Wave Number k

Profile	A	n
S1.0	0.003	2.48
S1.0 with cavities	0.003	2.59
S1.90	0.026	2.26
S2.0	0.004	2.27
S2.90	0.007	2.28

Presented in Figures 5a, 5b, and 7a and assuming $S(k) = A\,k^{-n}$ (equation (5)).

function of wave number, with best fit exponents having values of between 2.27 and 2.48.

4. Analysis of weighted composite spectra indicate an order of magnitude increase in sliding-related roughness measured perpendicular to the direction of ice flow relative to that measured parallel to ice flow. Slight changes in the orientation of glacier flow could, therefore, at least initially, result in significantly greater roughness-related, basal resistance over such surfaces.

5. Postglacial subaerial erosion tends to homogenize roughness with respect to orientation. Consequently, flow-parallel and flow-orthogonal roughnesses are less dissimilar after ~130 years of subaerial weathering than immediately following deglaciation. While net flow-parallel roughness approximately doubles with postglacial, subaerial weathering, flow-orthogonal roughness is approximately halved.

6. The influence of ice-bed separation is to reduce sliding-related roughness by between 27% and 43%, depending on the transition wave number used.

7. Increasing the transition wave number from 6.3 to 63 m^{-1} reduces net sliding-related roughness by ~80%, principally by reducing the influence of roughness elements at low wave numbers.

Acknowledgments. This work was supported by the University of Wales Academic Support Fund. Our thanks are extended to M. Sharp, K. Cuffey, A. Fountain, J. Andrews, F. Ng, J. Walder, and an anonymous referee for helpful advice and comments.

References

Benoist, J. -P., The spectral power density and shadowing function of a glacial microrelief at the decimeter scale, *J. Glaciol.*, *23*, 57-66, 1979.

Boulton, G. S., Processes of glacier erosion on different substrata, *J. Glaciol.*, 23, 15-38, 1979.

Cooley, J. W., and J. W. Tukey, An algorithm for the machine calculation of complex Fourier series, *Math. Comput.*, *19*, 297-301, 1965.

Cuffey, K., H. Conway, B. Hallet, A. M. Gades, and C. F. Raymond, Interfacial water in polar glaciers and glacier sliding at -17 °C, *Geophys. Res. Lett.*, *26*, 751-754, 1999.

Echelmeyer, K. and W. Zhongxiang, Direct observations of basal sliding and deformation of basal drift at sub-freezing temperatures, *J. Glaciol.*, *33*, 83-98, 1987.

Fairchild, I. J., L. Bradby, and B. Spiro, Carbonate diagenesis in ice, *Geology*, *21*(10), 901-904, 1993.

Geotronics Limited, Geodimeter, *Geodimeter News*, *3*, 8 pp., Huntingdon, England, 1995.

Hallet, B., Deposits formed by subglacial precipitation of $CaCO_3$, *Geol. Soc. Am. Bull.*, *87*, 1003-1015, 1976.

Hallet, B., A theoretical model of glacial abrasion, *J. Glaciol.*, 23(89), 39-50, 1979a.

Hallet, B., Subglacial regelation water film, *J. Glaciol.*, *23*, 321-334, 1979b.

Hallet, B., R. D. Lorrain, and R. Souchez, The composition of basal ice from a glacier sliding over limestones, *Geol. Soc. Am. Bull.*, *89*, 314-320, 1978.

Hubbard, B., and A. Hubbard, Bedrock surface roughness and the distribution of subglacially precipitated carbonate deposits: implications for formation at Glacier de Tsanfleuron, Switzerland, *Earth Surf. Processes Landforms*, *23*, 261-270, 1998.

Hubbard, B., and M. Sharp, Basal ice facies and their formation in the western Alps, *Arct. Alp. Res.*, *27*, 301-310, 1995.

Kamb, B., Sliding motion of glaciers: Theory and observation, *Rev. Geophys.*, *8*, 673-728, 1970.

Lemmens, M., R. Lorrain, and J. Haren, Isotopic composition of ice and subglacially precipitated calcite in an alpine area, *Z. Gletscherk.d Glazialgeol.*, *18*, 151-159, 1982.

McCarroll, D., A new instrument and techniques for the field measurement of rock surface roughness, *Z. Geomorphol.*, *36*, 69-79, 1992.

Nye, J. F., A calculation on the sliding of ice over a wavy surface using a Newtonian viscous approximation, *Proc. R. Soc. London, Ser. A*, *311*, 445-467, 1969.

Nye, J. F., Glacier sliding without cavitation in a linear viscous approximation, *Proc. R. Soc. London, Ser. A*, *315*, 381-403, 1970.

Nye, J. F., Water at the bed of the glacier. Association Internationale d'Hydrologie Scientifique Commission de Nieges et Glaces, in *Symposium on the Hydrology of Glaciers, Cambridge, 7-13 September 1969, IASH AISH Publ. 95*, 189-194, 1973.

Sharp, M. J., J. A. Dowdeswell, and J. C. Gemmell, Reconstructing past glacier dynamics and erosion from glacial geomorphic evidence: Snowdon, North Wales, *J. Quat. Sci.*, *4*, 115-130, 1989.

Sharp, M. J., J. -L. Tison, and G. Fierens, Geochemistry of subglacial calcites: implications for the subglacial hydrology of the basal water film, *Arct. Alp. Res.*, *22*, 141-152, 1990.

Souchez, R. A., and M. M. Lemmens, Subglacial carbonate deposition: an isotopic study of a present-day case, *Palaeogeogr. Palaeoclimatol. Palaeoecol.*, *51*, 357-364, 1985.

Tison, J. -L., and R. D. Lorrain, A mechanism of basal ice formation involving major ice-fabric changes, *J. Glaciol.*, *33*, 47-50, 1987.

Weertman, J., On the sliding of glaciers, *J. Glaciol.*, *3*, 33-38, 1957.

Weertman, J., The theory of glacier sliding, *J. Glaciol.*, *5*, 237-303, 1964.

B. Hubbard, Centre for Glaciology, Institute of Geography and Earth Sciences, University of Wales, Aberystwyth, Ceredigion SY23 3DB, Wales, U.K. (byh@aber. ac.uk)

D. McCarroll, Department of Geography, University of Wales, Swansea, West Glamorgan SA2 8PP, Wales, U.K. (D.McCarroll@swansea.ac.uk)

M. J. Siegert, Bristol Glaciology Centre, School of Geographical Sciences, University of Bristol, University Road, Bristol BS8 1SS, England, U.K. (m.j.siegert@bristol.ac.uk)

(Received July 20, 1999; revised January 20, 2000; accepted May 5, 2000.)